Finite-Set Model Predictive Power Control with Common Mode Voltage Elimination for an Asymmetrical Double-Star Induction Generator Wind Energy Conversion System

Yanis Hamoudi[1], Hocine Amimeur[1], Sabrina Nacef[1]
1- Laboratoire de Maitrise des Energies Renouvelables (LMER), Faculté de Technologie, Université de Bejaia, 06000 Bejaia, Algeria.
Email: yanis.hamoudi@univ-bejaia.dz (Corresponding author)
Email: hocine.amimeur@univ-bejaia.dz
Email: sabrina.nacef@univ-bejaia.dz

Received: 25 March 2023 Revised: 23 May 2023 Accepted: 17 June 2023

ABSTRACT:
The Finite-Set Model Predictive Power Control (FS-PPC) is one of the most intriguing model predictive approaches for the induction machine. This control is successful because it operates without weight coefficients and does not require the rotor flux position, as in the Predictive Torque Control (FS-PTC) and the Predictive Current Control (FS-PCC), respectively. A simple extension to the double-star induction generator results in significant current harmonics and common mode voltage. To fix these issues, this paper proposes an improved FS-PPC applied to an asymmetric double-star induction generator based wind energy conversion system by introducing two concepts: (a) the virtual voltage vector (VVV), in order to eliminate the (x, y) components of the stator currents. (b) the zero common mode voltage vectors (ZCMV), to eliminate the common mode voltage. A simulation of the developed ZCMV-FS-PPC system control is created in MATLAB/Simulink. The results show the effectiveness of this approach with CMV equal to zero and negligible (x, y) components of the stator currents. Moreover, the elimination of the CMV not only avoids its damage but also reduces the computation by 50%.

KEYWORDS: Predictive Power Control; Virtual Voltage Vector; Zero Common Mode Voltage; Double-Star Induction Generator; Wind Energy Conversion System.

1. INTRODUCTION

In the latest decade, Model Predictive Control (MPC) theory has emerged in electrical machines control. The newest control theory is capable of providing better flexibility and quicker dynamic response than traditional linear controllers [1]–[3]. The basic continuous set model predictive control (CS-MPC) suffers from high computation and complexity [4]. This problem has been fixed by the introduction of the Finite-Set Model Predictive Control (FS-MPC), exploiting the discrete character of the inverter's switching signal. This control is based on an online optimization of a cost function to determine the best voltage vector. Which is applied directly to the inverter without the need for modulation [5]. The most applied induction machine control is the predictive current control (FS-PCC) [6], [7] which is an excellent alternative to the classical Field-Oriented Control (FOC). This last one suffers from the linear inner current loop control. However, the FS-PCC control still needs the rotor flux position. Therefore, researchers are oriented towards Predictive Torque Control (FS-PTC) [8]–[10] as an alternative to Direct Torque Control (DTC). This latter has the disadvantage of the hysteresis comparator, which causes large torque ripples. Nevertheless, the FS-PTC requires a complex weighting factor design for effective flux and torque control. Considering the shortcomings of FS-PCC and FS-PTC, a better control approach that is unaffected by flux position and weighting factor design must be explored further. These qualities cited above are available in FS-PPC.

The FS-PPC control technique relies on the prediction of future active and reactive power values, which allows it to be more flexible and to have a faster dynamic response. This control theory is more applied to the Double-Fed Induction Machine (DFIM), [11], [12] and in the Permanent Magnet Synchronous Generator (PMSG) control [13], [14]. Less study has been made on the induction generator because the coupling is strong between the rotor and stator flux [15],

Paper type: Research paper
DOI: 10.30486/mjee.2023.1983159.1102
How to cite this paper: Y. Hamoudi, H. Amimeur, and S. Nacef, **"Finite-Set Model Predictive Power Control with Common Mode Voltage Elimination for an Asymmetrical Double-Star Induction Generator Wind Energy Conversion System"**, *Majlesi Journal of Electrical Engineering*, Vol. 17, No. 3, pp. 125-136, 2023.

[16]. In 2021, the authors in [15] propose a preliminary idea of an FS-PPC for a three phase induction machine. Later, in 2023, experimental verification was completed and its application was expanded see [17]. This approach is adopted for our application.

A simple extension of the FS-PPC on the Asymmetric Dual Star Induction Generator (ADISG) causes high current harmonics on the (x, y) subspace. Because the cost function of this approach excludes the (x, y) current component. To overcome this problem, the virtual voltage vector (VVV) concept is integrated into the FS-PPC in this paper.

The VVV provides simple and effective (x, y) current component regulation without adding them to the cost function. This approach employs two voltage vectors, every simple period T_s, a large vector, and a medium-large vector, with the same direction in the (α, β) subspace but opposite components direction in the (x, y) subspace. To balance the difference in length, the large vector is applied for $0.27\ T_s$ while the medium-large vector is used for $0.73\ T_s$. In this case, the (x, y) component is theoretically equal to zero. This technique has proven its effectiveness in both FS-PCC [18]–[20] and FS-PTC for multi-phase induction machines [21], [22]. However, this approach has not yet been applied to the FS-PPC.

Moreover, the common mode voltage is another issue that can impair the ADSIG control performance, affecting both system stability and motor lifespan [23]–[25]. To address this issue, the Common Mode Voltages (CMV) are eliminated by removing the VVV that causes it, which are 7 VVV. Thus, our FS-PPC control uses only 6 VVV, reducing the computation by half.

The purpose of this study is the application and the adaptation of the FS-PPC control for the ADSIG wind energy conversion system described in Fig. 1, by making two improvements: (a) the virtual voltage vector; (b) zero common mode voltage. As a result the stator currents (x, y) components are minimized, and the common mode voltages are eliminated, moreover the computation is reduced by 50%.

The contributions of this article are detailed in the following objectives:

- The minimization of the x, y currents using the VVV concept.
- The elimination of the common mode voltages by removing the VVVs that cause them.

To organize and accompany the reader in a successive reading process, this document is organized along the following lines: Section 2 presents the ADSIG mathematical model. Section 3 is devoted to the presentation of the conventional predictive power control principle and its limitations. Section 4 is dedicated to the suggested ZCMV-FS-PPC theory and its application for ADSIG control. The grid-side inverter control theory and the LCL filter design are presented in section 5. The last section covers the simulation results interpretation and the performance analysis of the studied system controlled by the proposed ZCMV-FS-PPC control.

2. ASYMMETRIC DUAL STAR INDUCTION MACHINE MODELLING

The machine used is made up of two identical windings in the stator, shifted by 30 degrees. The rotor is a squirrel cage, but for simplicity, it is referred to as a short-circuited three-phase winding [26], [27].

$$\begin{cases} v_{s1} = r_{s1} i_{s1} + \frac{d}{dt}\varphi_{s1} \\ v_{s2} = r_{s2} i_{s2} + \frac{d}{dt}\varphi_{s2} \\ v_r = r_r i_r + \frac{d}{dt}\varphi_r - j\omega_r \varphi_r = 0 \end{cases} \quad (1)$$

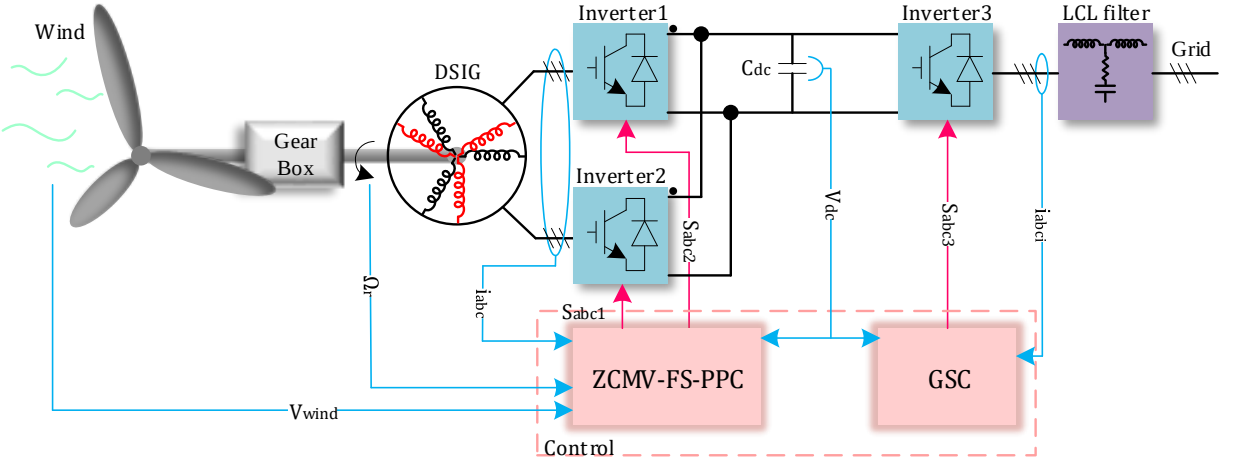

Fig. 1. ADSIG wind energy conversion system.

Where, $r_{sx}(x = 1,2)$; r_r: is the stator, rotor resistance; ω_r: the rotor electrical angular speed. All the other symbols stand for their usual meanings. The stator and rotor flux linkages are expressed as follows [28]:

$$\begin{cases} \varphi_{s1} = L_{ls1}\imath_{s1} + L_m(\imath_{s1} + \imath_{s2} + \imath_r) \\ \varphi_{s1} = L_{ls2}\imath_{s2} + L_m(\imath_{s1} + \imath_{s2} + \imath_r) \\ \varphi_r = L_{lr}\imath_r + L_m(\imath_{s1} + \imath_{s2} + \imath_r) \end{cases} \quad (2)$$

Typically, vector space decomposed voltages are used to investigate multiphase machines. After using the Clarke transformation [29], we obtain the ADSIM model in the $(\alpha - \beta\,; x - y)$ subspace:

$$\begin{cases} v_{\alpha s} = r_s\imath_{\alpha s} + \dfrac{d}{dt}\varphi_{\alpha s} \\ v_{\beta s} = r_s\imath_{\beta s} + \dfrac{d}{dt}\varphi_{\beta s} \\ v_{xs} = r_s\imath_{xs} + \dfrac{d}{dt}\varphi_{xs} \\ v_{ys} = r_s\imath_{ys} + \dfrac{d}{dt}\varphi_{ys} \\ v_{\alpha r} = r_r\imath_{\alpha r} + \dfrac{d}{dt}\varphi_{\alpha r} + \omega_r\varphi_{\beta r} = 0 \\ v_{\beta r} = r_r\imath_{\beta r} + \dfrac{d}{dt}\varphi_{\beta r} - \omega_r\varphi_{\alpha r} = 0 \end{cases} \quad (3)$$

Where, r_s; r_r: the stator, rotor resistance; ω_r: the electrical angular speed of the rotor. All of the other symbols represent their regular meanings. The stator and rotor flux linkages are expressed as follows [30]:

$$\begin{cases} \varphi_{\alpha s} = L_{ls}\imath_{\alpha s} + L_m(\imath_{\alpha s} + \imath_{\alpha r}) \\ \varphi_{\beta s} = L_{ls}\imath_{\beta s} + L_m(\imath_{\beta s} + \imath_{\beta r}) \\ \varphi_{xs} = L_{ls}\imath_{xs} \\ \varphi_{ys} = L_{ls}\imath_{ys} \\ \varphi_{\alpha r} = L_{lr}\imath_{\alpha r} + L_m(\imath_{\alpha s} + \imath_{\alpha r}) \\ \varphi_{\beta r} = L_{lr}\imath_{\beta r} + L_m(\imath_{\beta s} + \imath_{\beta r}) \end{cases} \quad (4)$$

Where, L_{ls} ; L_{lr}: The stator, rotor leakage inductance, L_m: The magnetizing inductance.

The electromagnetic torque is written as follows:

$$T_{em} = P\, Im\{\varphi_s^*\, \imath_s\} \quad (5)$$

The mechanical equation of the machine is defined as follows:

$$T_{em} - T_g = J\frac{\mathrm{d}\Omega}{\mathrm{dt}} + f\Omega \quad (6)$$

3. CONVENTIONAL MODEL PREDICTIVE POWER CONTROL

This section introduces the basic concept and control structure of the conventional FS-PPC used in the ADSIG control. This control represents one of the most fascinating models of predictive control approaches. Its success is due to the fact that it operates without weight coefficients, unlike the FS-PTC, and does not require flux rotor position, as in the FS-PCC.

The FS-PPC control is implemented in three steps:

1- First, the stator and rotor flux values and the machine speed are estimated.

2- In the second phase, the ADSIG active and reactive power and the stator flux value are predicted using the stator currents. The prediction is done using the forward Euler discretization of the continuous ADSIG model as illustrated in Equations 7-10.

$$\begin{cases} \varphi_{s1}^p(k+1) = \varphi_{s1}(k) + T_s\, v_{s1}(k) - T_s r_{s1}\, i_{s1}(k) \\ \varphi_{s2}^p(k+1) = \varphi_{s2}(k) + T_s\, v_{s2}(k) - T_s r_{s2}\, i_{s2}(k) \end{cases} \quad (7)$$

$$\begin{cases} \imath_{s1}^p(k+1) = (1 - T_s/\tau_{\sigma 1})\,\imath_{s1}(k) + \\ \dfrac{T_s}{R_{\sigma 1}(\tau_{\sigma 1}+T_s)}\left[k_r\left(\dfrac{1}{\tau_r} + j\omega_r(k)\right)\varphi_r(k) + v_{s1}(k)\right] \\ \imath_{s2}^p(k+1) = (1 - T_s/\tau_{\sigma 2})\,\imath_{s2}(k) + \\ \dfrac{T_s}{R_{\sigma 2}(\tau_{\sigma 2}+T_s)}\left[k_r\left(\dfrac{1}{\tau_r} + j\omega_r(k)\right)\varphi_r(k) + v_{s2}(k)\right] \end{cases} \quad (8)$$

Where, $R_{\sigma i} = R_{si} + R_r k_r^2$; $\tau_{\sigma i} = \frac{\sigma(L_{lsi}+L_m)}{R_{\sigma i}}$; $k_r = \frac{L_m}{L_r}$; $\sigma_i = 1 - \left(\frac{{L_m}^2}{(L_{lsi}+L_m)L_r}\right)$. With $i = 1; 2$

$$\begin{cases} P_{em1}^p(k+1) = \omega_r(k)\, Im\left\{\varphi_{s1}^*(k+1)\,\imath_{s1}^p\,(k+1)\right\} \\ P_{em2}^p(k+1) = \omega_r(k)\; Im\left\{\varphi_{s2}^*(k+1)\,\imath_{s2}^p\,(k+1)\right\} \end{cases} \quad (9)$$

$$\begin{cases} Q_{em1}^{p}(k+1) = \omega_r(k)\ Re\left\{\varphi_{s1}^{*}(k+1)\, \iota_{s1}^{p}\,(k+1)\right\} \\ Q_{em2}^{p}(k+1) = \omega_r(k)\ Re\left\{\varphi_{s2}^{*}(k+1)\, \iota_{s2}^{p}\,(k+1)\right\} \end{cases} \quad (10)$$

3-The last step is the multi-objective optimization of the cost function $g_{i,}(i = 1; 2)$, to determine the VVV applied at each simple period Equation 11.

$$\begin{cases} g_1 = \left|P_{em1}^{*} - P_{em1}^{p}\right| + \left|Q_{em1}^{*} - Q_{em1}^{p}\right| \\ g_2 = \left|P_{em2}^{*} - P_{em2}^{p}\right| + \left|Q_{em2}^{*} - Q_{em2}^{p}\right| \end{cases} \quad (11)$$

To simplify the previous steps, a synoptic diagram is seen in Fig. 2. The active and reactive power reference values P_{em1}^{*}, P_{em2}^{*}, and Q_{em1}^{*}, Q_{em2}^{*} in the FS-PPC control provided by the external loops are: The speed regulation loop to assure the MPPT, and the rotor flux regulation loop respectively.

4. PROPOSED VIRTUAL VOLTAGE VECTORS PREDICTIVE POWER CONTROL

A simple extension of the three phase FS-PPC approach to an ADISG results in substantial current harmonics.

An adaptation is necessary by introducing the VVV concept in such a way as to assure power control and eliminate the(x, y) components of the stator currents. Moreover, the common mode voltage can impair the ADSIG control performance, affecting both system stability and motor lifespan [23]–[25]. The following subtitles address the two issues.

4.1. Virtual Voltage Vectors

With a two-level six-phase inverter, it is possible to apply 64 vectors to an ADSIG, 49 of which are different. These vectors are distributed as follows: 12 large vectors, 12 medium-large vectors, 12 medium vectors, 12 small vectors, and one null vector. Each applied voltage vector will have one component in the (α, β) subspace and another component in the (x, y) subspace, see Fig. 3. To eliminate the (x, y) component, two voltage vectors are applied at each sample period T_s, a large vector, and a medium-large vector. These two vectors are chosen so that their two (x, y) components opposite, for example, $V52$ and $V38$, see Fig. 3. To adjust the magnitude difference between the two vectors, we apply $V52$ during $0.73\ T_s$, and $V38$ during $0.27\ T_e$. The general form is given as follows:

$$VVV_i = 0.73\ V_{large} + 0.27\ V_{medium-large} \quad (12)$$

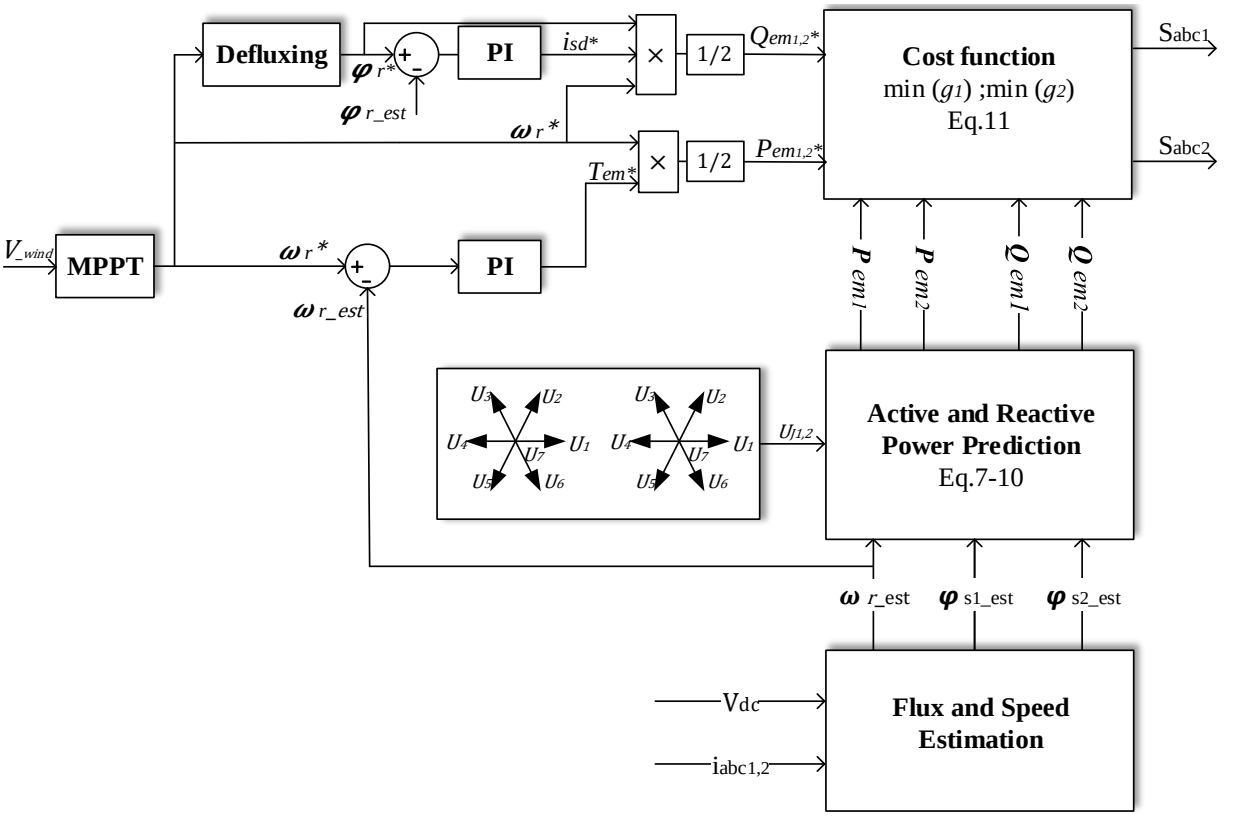

Fig. 2. Conventional FS-PPC control block diagram.

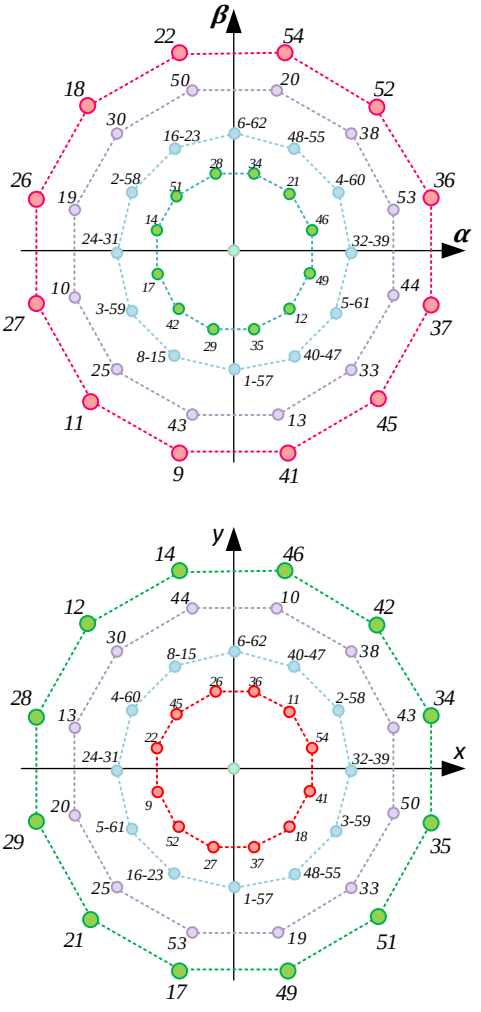

Fig. 3. Voltage vectors in the $\alpha-\beta$; $x-y$ subspaces for an ADSIG.

4.2. Zero Common-Mode Voltage

The CMV in the ADSIG is designated as the sum of the six pole voltages, calculated as follows:

$$V_{CMV} = \frac{V_{dc}}{6}\,(S_a + S_b + S_c + S_u + S_v + S_w) \qquad (13)$$

In 64 voltage vectors possible, there are 20 voltage vectors with zero common-mode voltages: $V_{07}, V_{13}, V_{15}, V_{16}, V_{23}, V_{25}, V_{26}, V_{31}, V_{32}, V_{34}, V_{43}, V_{45}, V_{46}, V_{51}, V_{52}, V_{54}, V_{61}, V_{62}, V_{64}, V_{70}$. Where 6 are large and 6 are medium-large, producing 6 VVV used in this approach. The other voltage vectors generate shaft voltage and leakage current components, causing electromagnetic interference and affecting normal operation [25]. For this reason, these vectors are removed, leaving only 6 VVV to be used in the FS-PPC control, see Fig. 4.

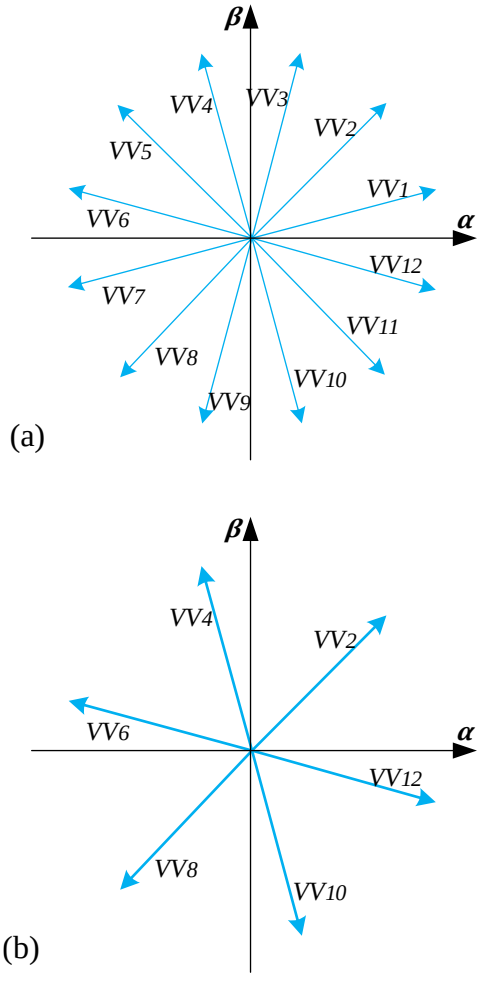

Fig. 4. VVV in the $\alpha-\beta$ subspace for an ADSIG (a) with the common-mode voltage (b) without CMV.

To apply the VVV in the FS-PPC control, we use the model of the ADSIG in the $(\alpha-\beta)$, $(x-y)$ subspaces presented in section 2. The modifications made to the FS-PPC are as follows:

1-The prediction of the total active and reactive power, through the currents and flux value. This prediction is made using the forward Euler discretization of the ADSIG model presented in section 2 (equations 2 - 5) as shown in Equations 14 -17.

$$\varphi_s^p(k+1) = \varphi_s(k) + T_s[v_s(k) - r_s\, i_s(k)] \qquad (14)$$

$$\iota_s^p(k+1) = \frac{T_s}{R_\sigma(\tau_\sigma+T_s)}\left[k_r\left(\frac{1}{\tau_r} + j\omega_r(k)\right)\varphi_r(k) + v_s(k)\right] + (1 - T_s/\tau_\sigma)\iota_s(k) \qquad (15)$$

Where, $R_\sigma = R_s + R_r k_r^2$; $\tau_\sigma = \frac{\sigma(L_{ls}+L_m)}{R_\sigma}$;

$k_r = \frac{L_m}{L_r}$; $\sigma = 1 - \left(\frac{{L_m}^2}{(L_{ls}+L_m)L_r}\right)$.

$$P_{em}^{p}(k+1) = \omega_r(k)\, Im\{\varphi_s^*(k+1)\, \iota_s^{p}\,(k+1)\} \quad (16)$$

$$Q_{em}^{p}(k+1) = \omega_r(k)\, Re\{\varphi_s^*(k+1)\, \iota_s^{p}\,(k+1)\} \quad (17)$$

2-In this control, one cost function is used as shown in Equation 18.

$$g = |P_{em}^{*} - P_{em}^{p}| + |Q_{em}^{*} - Q_{em}^{p}| \quad (18)$$

Fig. 5 depicts the proposed ZCMV-FS-PPC synoptic diagram, with the modifications denoted by red boxes.

5. GRID CONNECTION

After controlling the ADSIG to deliver the MPPT, this section will discuss the control used to transport this energy to the 230/400 V, 50 Hz electrical grid. The approach employed is described in Fig. 6, for more details consulted [31]. Moreover, an *LCL* filter is used to reduce the harmonics generated by the inverter.

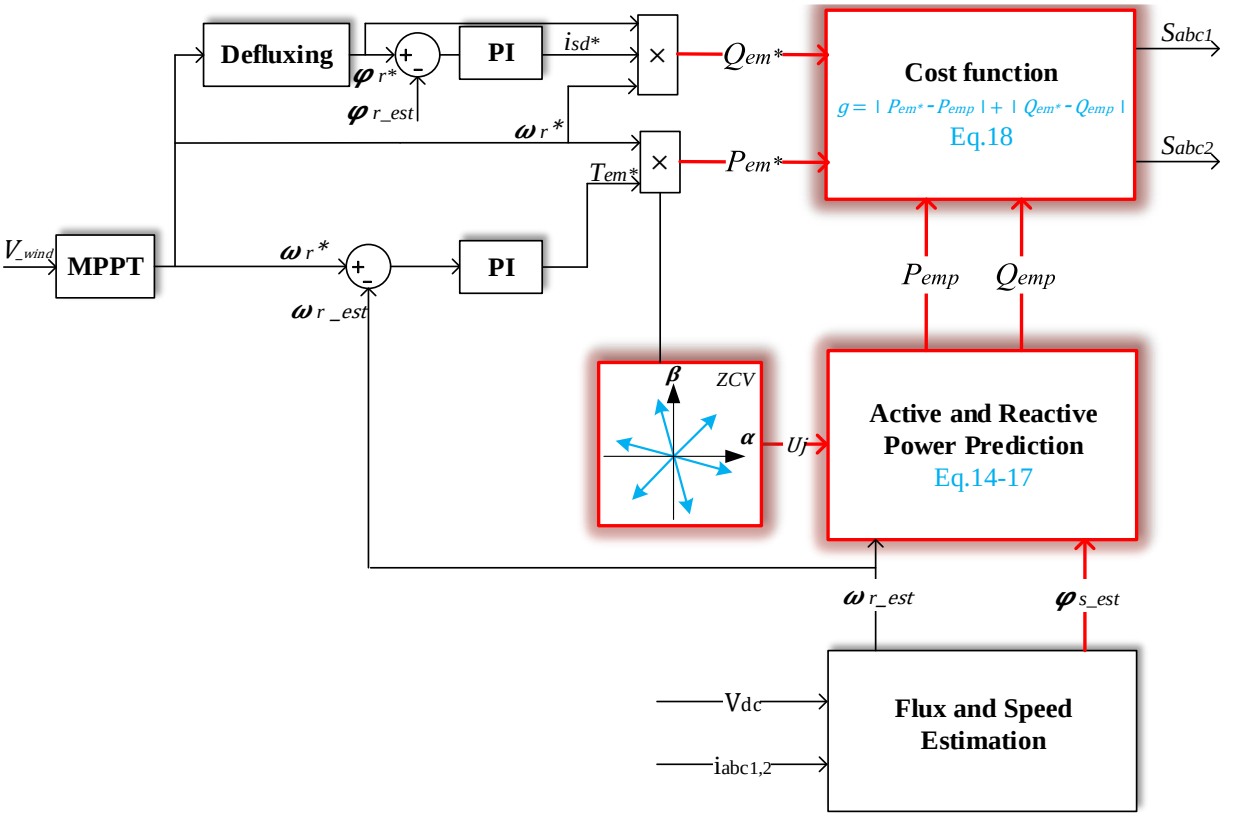

Fig. 5. Proposed control block diagram ZCMV-FS-PPC.

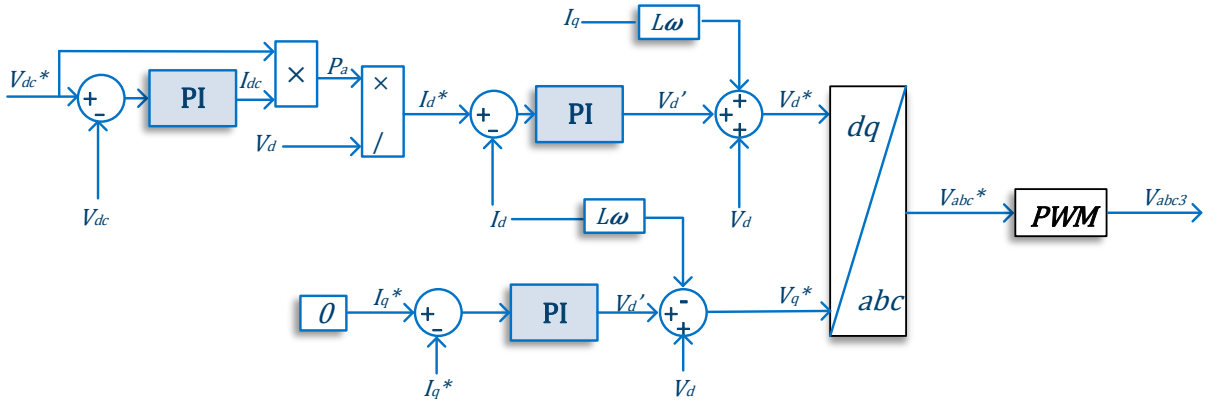

Fig. 6. Grid connection conditioning system's control bloc diagram.

While designing the *LCL* filter, we need to consider the filter size, current ripple, and switching attenuation. The *LCL* filter consists of the inverter-side inductance L_i , the grid-side inductance L_g, and a capacitor C_f. To avoid resonance with the grid, a resistance R_d is placed in series with the capacitor [32]. see Fig. 7. The *LCL* filter parameters are determined as follows:
1- The filter values are expressed as a percentage of the flowing base values:

$$\begin{cases} L_b = \dfrac{U_n^2}{\omega_g P_n} \\ C_b = \dfrac{1}{{\omega_g}^2 L_b} \end{cases} \tag{19}$$

2-With 2.7% of the base inductance, the inverter side inductance can reduce the current ripple to 10%, and by adding the *LC* part, these harmonics can be reduced to 2% [33].

$$\begin{cases} L_i = L_b\, 2.7\% \\ L_g = r\, L_i \end{cases} \tag{20}$$

With $r = 1.2$ to reduce the damping resistor effect.

3-The grid accepts 5% of the maximum power factor variation, which is equivalent to 5% of the base capacitance.

$$C_f = 0.05\, C_b \tag{21}$$

4-The resonant frequency and damping resistor are computed respectively as follows:

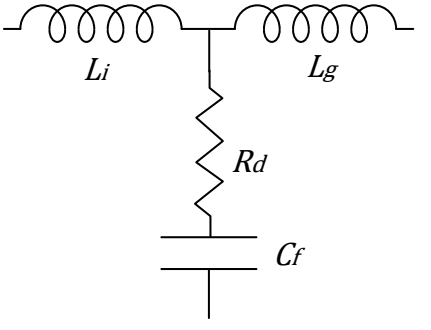

Fig. 7. LCL filter

$$f_{res} = \frac{1}{2\pi}\sqrt{\frac{L_i + L_g}{L_i L_g C_f}} \tag{22}$$

$$R_d = \frac{1}{3\omega_{res} C_f} \tag{23}$$

The LCL filter parameter values determined are:
$L_i = 3.05\ mH$; $L_g = 3.67\ mH$; $C_f = 4.48\ \mu F$;
$R_d = 6.43\ \Omega$; $f_{res} = 1.84\ kHz$

6. ZCMV-FS-PPC SIMULATION RESULTS

6.1. Comparative test

In this part, the performance of the proposed control ZCMV-FS-PPC is compared with the traditional simple extension FS-PPC, and the VVV-FS-PPC in the case of a constant wind speed equal to 10 m/s.

Fig. 8 shows the steady-state performance test of three different controls, where the left one represents a simple extension of the conventional FS-PPC, the middle the FS-PPC + VVV, and the right the FS-PPC + VVV + ZCMV.

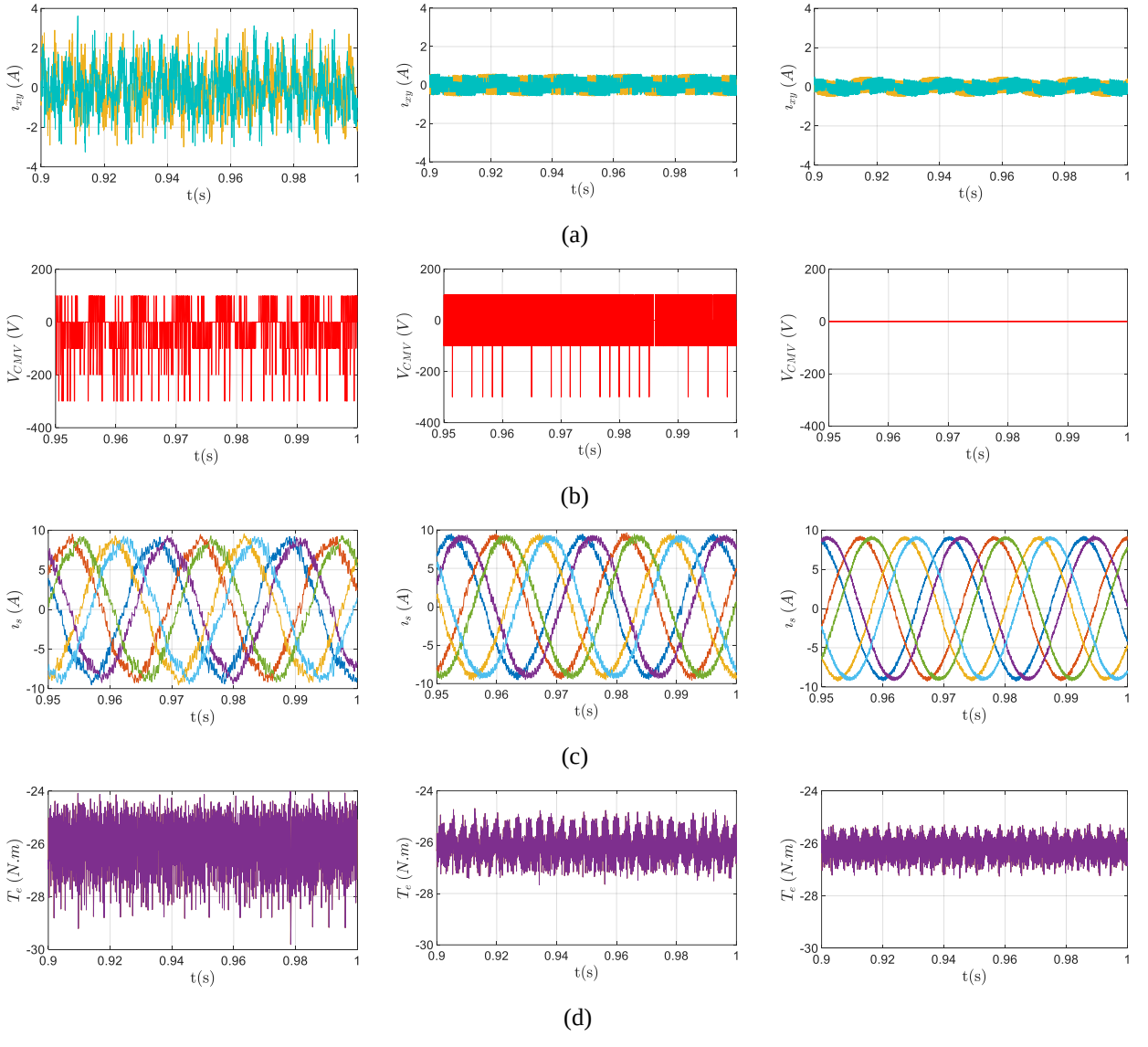

Fig. 8. Steady-state performance from lift to right: FS-PPC; VVV-FS-PPC; ZCMV-FS-PPC. From top to bottom. (a) (x,y) currents; (b) common mode voltage ;(c) stator currents ;(d) electromagnetic torque.

We can observe that the simple extension of the traditional FS-PPC produces large x, y currents of 3 A and a common mode voltage of 300 V. Which impacts the stator current quality and induces important torque ripples of 6 N.m.

With the introduction of the VVV concept, the (x, y) current components are reduced to 0.6 A, allowing for an improvement in the current quality (c) and a reduction in torque ripple to less than 2.5 N.m. But the common mode voltage is still there.

In the proposed control (right), the x, y currents are reduced to 0.4 A and the common mode voltage is attenuated (equal to 0); consequently, the current quality is improved and the torque ripples are reduced to 1.5 N.m. Which reflects the superiority of the suggested control.

6.2. Performance Test Under Wind Speed Variation

The simulation results of the wind power conversion system with the proposed ZCMV-FS-PPC control are discussed in this part. The wind is simulated in its natural intermittent behavior via a variable profile presented in Fig. 9. This system provides power directly to the grid.

Fig. 10 presents the ADSIG rotor speed controlled to track the speed reference provided by the MPPT bloc. It is clear that the ADSIG speed is well controlled therefore the MPPT is ensured with an energy efficiency of 0.438, as seen in Fig. 11.

In Fig. 12 and 13, we can see that the currents are sinusoidal and have good quality. Thanks to the $(x,\ y)$

current harmonic reduced with the VVV technique with a maximum value of 0.5 A, see Fig. 14.

The common mode voltage of the ADSIG is shown in Fig. 15. The CMV is completely removed, resulting in a lower torque ripple as can be seen in Fig. 16. demonstrating the validity of the ZCM strategy used.

Fig. 17 illustrates the direct and quadratic rotor flux. It can be observed that the rotor flux is perfectly orientated on the direct axis, without having the rotor position, which favors FS-PPC over FS-PCC.

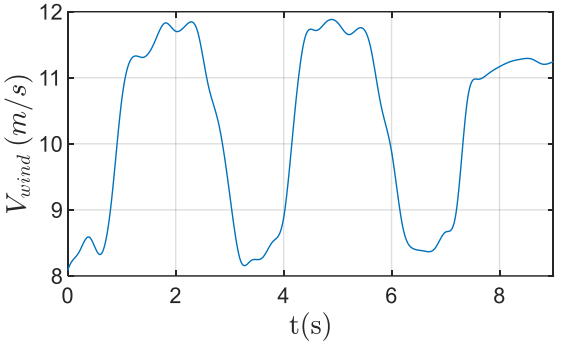

Fig. 9. Wind speed profile.

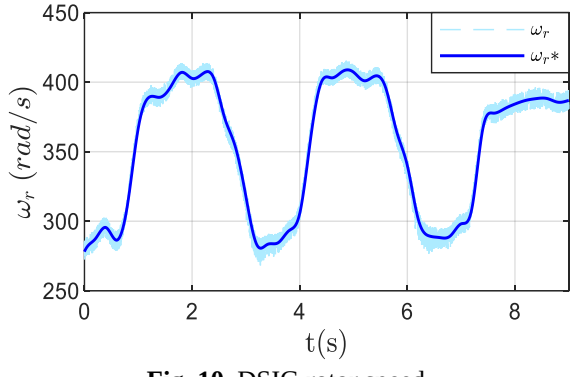

Fig. 10. DSIG rotor speed.

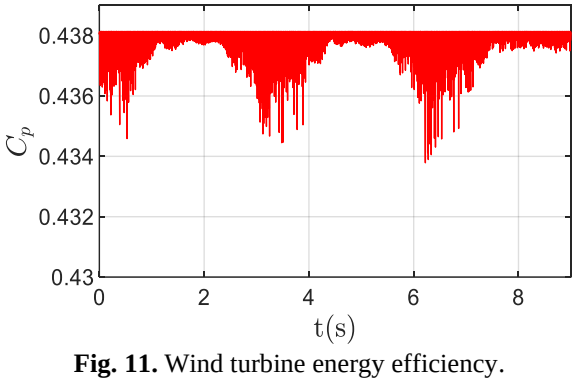

Fig. 11. Wind turbine energy efficiency.

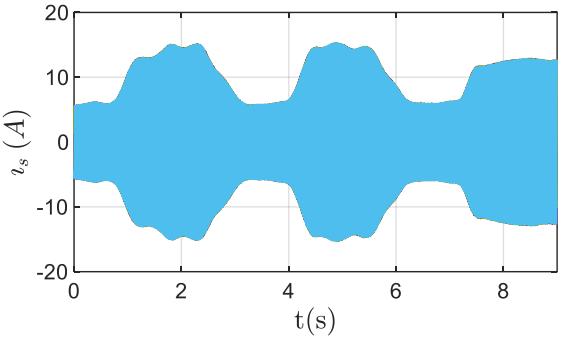

Fig. 12. ADSIG stator currents.

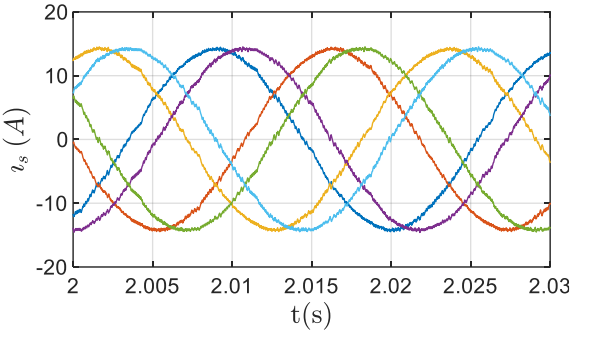

Fig. 8. Zoom in DSIG stator currents.

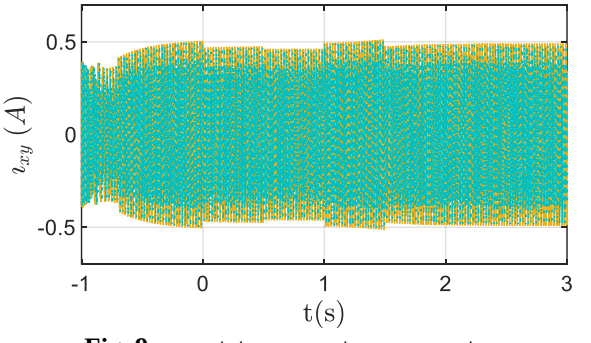

Fig. 9. x, y stator current components.

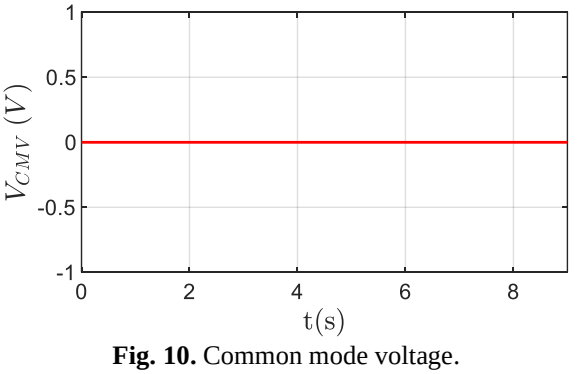

Fig. 10. Common mode voltage.

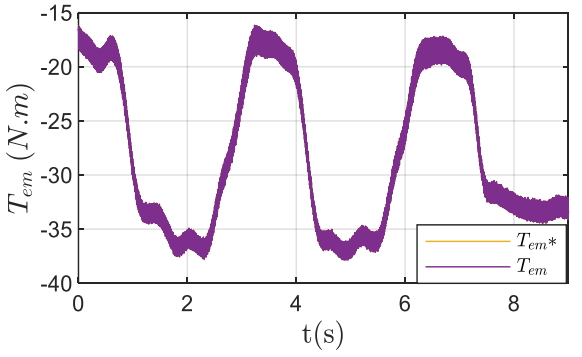

Fig. 16. Electromagnetic torque of the two stator windings.

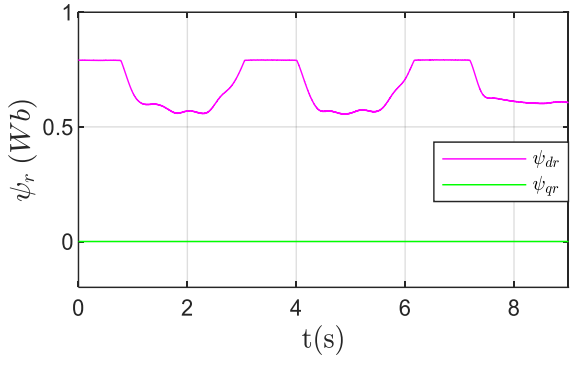

Fig. 17. Direct and quadratic rotor flux.

On the other hand, the grid-side converter (GSC) is controlled to ensure the total transfer of the active power produced to a 230/400 V; 50 Hz grid. The DC link voltage is adjusted to 600 V with a PI controller throw the active power. While the reactive power is set to zero to avoid the reactive exchange with the grid.

Fig. 18 depicts the DC link voltage control. The DC link voltage is regulated on 600V with a maximum error of 0.06 % which is a satisfactory result.

Fig. 19 demonstrates the active and reactive power injected into the grid. According to this Fig., the highest active power transferred to the grid is 3.8 kW, and no reactive power is exchanged with the grid, which is a desirable outcome.

The grid voltage and current are given in Fig.s 20 and 21. A high-quality signal is obtained with a 2.28% harmonic distortion rate of the grid current as shown in Fig. 22, thanks to the control and the *LCL* filter. The voltage is set to 230 V, and there is no shift between the current and the voltage.

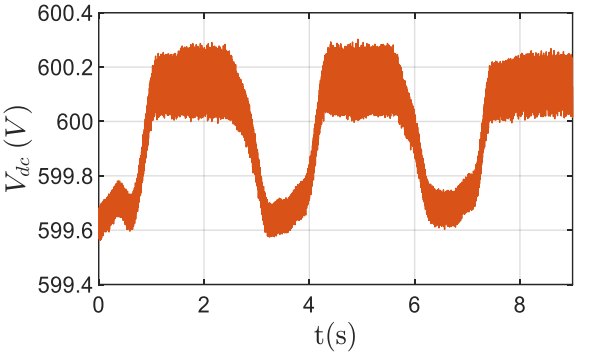

Fig. 18. DC link voltage.

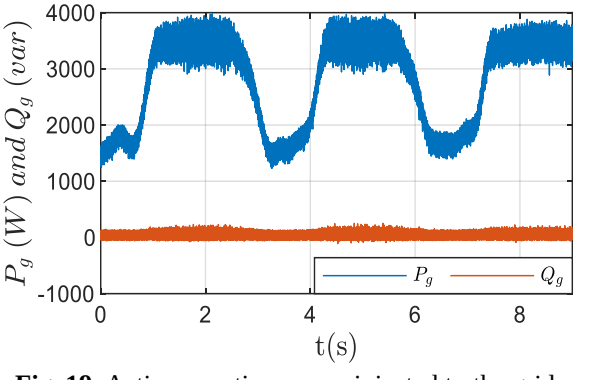

Fig. 19. Active, reactive power injected to the grid.

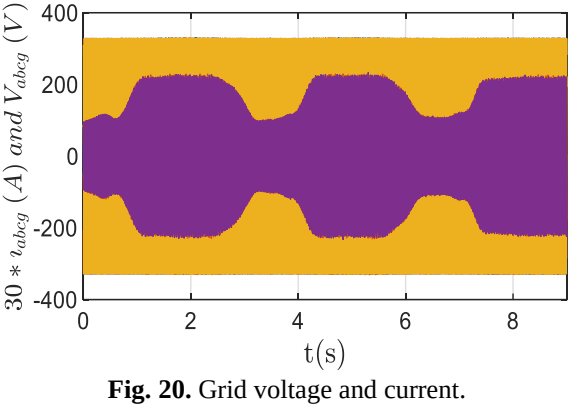

Fig. 20. Grid voltage and current.

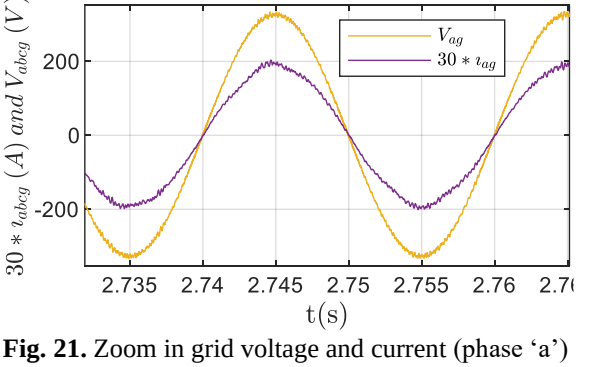

Fig. 21. Zoom in grid voltage and current (phase 'a')

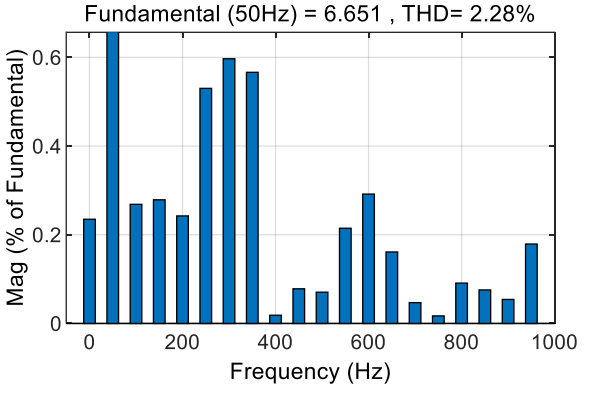

Fig. 22. Grid current harmonic.

7. CONCLUSION

This work is devoted to the FS-PPC application for a variable speed ADSIG wind energy conversion system to avoid the problem of the flux position required in FS-PCC and the weighting factor design required in FS-PTC. The challenges encountered are the stator current harmonics and the CMV. For this purpose, two concepts are introduced: the virtual voltage vector, and the common mode voltage elimination. As a result, the proposed ZCMV-FS-PPC control presents the simplest control that works without rotor flux position and without weighting factor. Moreover, the computation is reduced to less than 50%, the common mode voltage is completely eliminated, and the (x, y) current components are kept less than 0.5 A under a simple period $T_S = 30\mu s$.

This study may have these perspectives, the experimental confirmation of the suggested ZCMV-FS-PPC approach; replacing the external PI controllers with non-linear controllers to have more flexibility; and analyzing this control performance under fault conditions.

8. ACKNOWLEDGMENT

We are grateful to Algeria's DGRSDT for providing our laboratory with the required subventions.

REFERENCES

[1] J. Rodas, I. Gonzalez-Prieto, Y. Kali, M. Saad, and J. Doval-Gandoy, **"Recent Advances in Model Predictive and Sliding Mode Current Control Techniques of Multiphase Induction Machines,"** *Front. Energy Res.*, vol. 9, no., pp. 1-22 Aug. 2021, doi: 10.3389/fenrg.2021.729034.

[2] I. Merzouk, K. Bdirina, and M. L. Bendaas, **"Finite set model predictive control of PWM AC/DC converter with virtual-flux estimation under grid imbalance,"** *Majlesi J. Electr. Eng.*, vol. 13, no. 2, pp. 111–119, 2019.

[3] M. Ayala, J. Doval-Gandoy, J. Rodas, O. Gonzalez, R. Gregor, and M. Rivera, **"A Novel Modulated Model Predictive Control Applied to Six-Phase Induction Motor Drives,"** *IEEE Trans. Ind. Electron.*, vol. 68, pp. 3672–3682, May 2021, doi: 10.1109/TIE.2020.2984425.

[4] F. Wang, Z. Zhang, X. Mei, J. Rodríguez, and R. Kennel, **"Advanced Control Strategies of Induction Machine: Field Oriented Control, Direct Torque Control and Model Predictive Control,"** *Energies*, vol. 11, no. 1, p. 120, Jan. 2018, doi: 10.3390/en11010120.

[5] M. F. Elmorshedy, W. Xu, F. F. M. El-Sousy, M. R. Islam, and A. A. Ahmed, **"Recent Achievements in Model Predictive Control Techniques for Industrial Motor: A Comprehensive State-of-the-Art,"** *IEEE Access*, vol. 9, pp. 58170–58191, 2021, doi: 10.1109/ACCESS.2021.3073020.

[6] A. Habib, A. Shawier, M. Mamdouh, A. Samy Abdel-Khalik, M. S. Hamad, and S. Ahmed, **"Predictive current control based pseudo six-phase induction motor drive,"** *Alexandria Eng. J.*, vol. 61, no. 5, pp. 3937–3948, May 2022, doi: 10.1016/j.aej.2021.09.015.

[7] J. Serra, I. Jlassi, and A. J. M. Cardoso, **"A computationally efficient model predictive control of six-phase induction machines based on deadbeat control,"** *Machines*, vol. 9, no. 12, 2021, doi: 10.3390/machines9120306.

[8] M. S. Mousavi *et al.*, **"Predictive Torque Control of Induction Motor Based on a Robust Integral Sliding Mode Observer,"** *IEEE Trans. Ind. Electron.*, vol. 70, no. 3, pp. 2339–2350, Mar. 2023, doi: 10.1109/TIE.2022.3169831.

[9] Z. Li, J. Xia, X. Gao, Y. Guo, and X. Zhang, **"Dual-Vector-Based Predictive Torque Control for Fault-Tolerant Inverter-Fed Induction Motor Drives With Adaptive Switching Instant,"** *IEEE Trans. Ind. Electron.*, pp. 1–10, 2023, doi: 10.1109/TIE.2023.3236088.

[10] Z. Li, J. Xia, X. Gao, J. Rodriguez, Y. Guo, and X. Zhang, **"Modulated Model Predictive Torque Control for Fault-Tolerant Inverter-Fed Induction Motor Drives With Single DC-Link Voltage Sensor,"** *IEEE Trans. Power Electron.*, pp. 1–12, 2023, doi: 10.1109/TPEL.2023.3267078.

[11] A. Benzouaoui, H. Khouidmi, and B. Bessedik, **"Parallel model predictive direct power control of DFIG for wind energy conversion,"** *Int. J. Electr. Power Energy Syst.*, vol. 125, no. August 2020, p. 106453, Feb. 2021, doi: 10.1016/j.ijepes.2020.106453.

[12] X. Wei, M. Cheng, J. Zhu, H. Yang, and R. Luo, **"Finite-Set Model Predictive Power Control of Brushless Doubly Fed Twin Stator Induction Generator,"** *IEEE Trans. Power Electron.*, vol. 34, no. 3, pp. 2300–2311, Mar. 2019, doi: 10.1109/TPEL.2018.2845129.

[13] J. Ji, S. Jin, W. Zhao, D. Xu, L. Huang, and X. Qiu, **"Simplified Three-Vector-Based Model Predictive Direct Power Control for Dual Three-Phase PMSG,"** *IEEE Trans. Energy Convers.*, vol. 37, no. 2, pp. 1145–1155, Jun. 2022, doi: 10.1109/TEC.2021.3131961.

[14] B. Majout *et al.*, **"A Review on Popular Control**

Applications in Wind Energy Conversion System Based on Permanent Magnet Generator PMSG," *Energies*, vol. 15, no. 17, p. 6238, Aug. 2022, doi: 10.3390/en15176238.

[15] J. Zhang *et al.*, **"Predictive Power Control of Induction Motor Drives,"** in *2021 IEEE International Conference on Predictive Control of Electrical Drives and Power Electronics (PRECEDE)*, Nov. 2021, pp. 524–529, doi: 10.1109/PRECEDE51386.2021.9681051.

[16] J. Zhang, H. Li, Z. Li, and Z. Zhang, **"Predictive Power Factor Control of Induction Motor Drives,"** in *2022 International Symposium on Power Electronics, Electrical Drives, Automation and Motion (SPEEDAM)*, Jun. 2022, pp. 106–111, doi: 10.1109/SPEEDAM53979.2022.9842246.

[17] J. Zhang, Z. Zhang, X. Liu, Z. Li, and O. Babayomi, **"Predictive power control of induction motor drives with improved efficiency,"** *Energy Reports*, vol. 9, no. April, pp. 496–503, Apr. 2023, doi: 10.1016/j.egyr.2023.03.053.

[18] A. Gonzalez-Prieto, I. Gonzalez-Prieto, and M. J. Duran, **"Smart Voltage Vectors for Model Predictive Control of Six-Phase Electric Drives,"** *IEEE Trans. Ind. Electron.*, vol. 68, no. 10, pp. 9024–9035, Oct. 2021, doi: 10.1109/TIE.2020.3028812.

[19] O. Gonzalez *et al.*, **"Model Predictive Current Control of Six-Phase Induction Motor Drives Using Virtual Vectors and Space Vector Modulation,"** *IEEE Trans. Power Electron.*, vol. 37, no. 7, pp. 7617–7628, Jul. 2022, doi: 10.1109/TPEL.2022.3141405.

[20] J. Aciego, A. Gonzalez-Prieto, I. Gonzalez-Prieto, A. Claros, M. J. Duran, and M. Bermudez, **"On the Use of Predictive Tools to Improve the Design of Undergraduate Courses,"** *IEEE Access*, vol. 10, no. December, pp. 3105–3115, 2022, doi: 10.1109/ACCESS.2021.3139803.

[21] H. Xu, L. Chen, and X. Sun, **"MPTC of a six-phase PMSHM with auxiliary voltage vectors,"** *Int. J. Appl. Electromagn. Mech.*, vol. 65, no. 4, pp. 763–779, Apr. 2021, doi: 10.3233/JAE-201550.

[22] Z. Zhang, Q. Sun, Q. Di, and Y. Wu, **"A Predictive Torque Control Method for Dual Three-Phase Permanent Magnet Synchronous Motor Without Weighting Factor,"** *IEEE Access*, vol. 9, pp. 112585–112595, 2021, doi: 10.1109/ACCESS.2021.3104301.

[23] A. M. Alcaide *et al.*, **"Common-Mode Voltage Mitigation of Dual Three-Phase Voltage Source Inverters in a Motor Drive Application,"** *IEEE Access*, vol. 9, pp. 67477–67487, 2021, doi: 10.1109/ACCESS.2021.3072967.

[24] Z. Shen, D. Jiang, Z. Liu, D. Ye, and J. Li, **"Common-Mode Voltage Elimination for Dual Two-Level Inverter-Fed Asymmetrical Six-Phase PMSM,"** *IEEE Trans. Power Electron.*, vol. 35, no. 4, pp. 3828–3840, Apr. 2020, doi: 10.1109/TPEL.2019.2933446.

[25] Q. Yuan, R. Zhao, R. Xiao, and Z. Liu, **"Zero Common-Mode Voltage Model Predictive Torque Control Based on Virtual Voltage Vectors for the Dual Three-Phase PMSM Drive,"** *Electronics*, vol. 11, no. 20, p. 3293, Oct. 2022, doi: 10.3390/electronics11203293.

[26] H. Khouidmi, A. Benzouaoui, and B. Bessedik, **"Sliding-mode MRAS speed estimator for sensorless vector control of double stator induction motor,"** *Majlesi J. Electr. Eng.*, vol. 12, no. 3, pp. 41–53, 2018.

[27] M. Nesri, K. Nounou, K. Marouani, A. Houari, and M. F. Benkhoris, **"Efficiency improvement of a vector-controlled dual star induction machine drive system,"** *Electr. Eng.*, vol. 102, no. 2, pp. 939–952, Jun. 2020, doi: 10.1007/s00202-020-00924-9.

[28] A. Guettab, Z. Boudjema, E. Bounadja, and R. Taleb, **"Improved control scheme of a dual star induction generator integrated in a wind turbine system in normal and open-phase fault mode,"** *Energy Reports*, vol. 8, pp. 6866–6875, Nov. 2022, doi: 10.1016/j.egyr.2022.05.048.

[29] J. J. Aciego, I. Gonzalez Prieto, and M. J. Duran, **"Model Predictive Control of Six-Phase Induction Motor Drives Using Two Virtual Voltage Vectors,"** *IEEE J. Emerg. Sel. Top. Power Electron.*, vol. 7, no. 1, pp. 321–330, 2019, doi: 10.1109/JESTPE.2018.2883359.

[30] J. K. Pandit, M. V. Aware, R. V. Nemade, and E. Levi, **"Direct Torque Control Scheme for a Six-Phase Induction Motor With Reduced Torque Ripple,"** *IEEE Trans. Power Electron.*, vol. 32, no. 9, pp. 7118–7129, Sep. 2017, doi: 10.1109/TPEL.2016.2624149.

[31] H. Amimeur, D. Aouzellag, R. Abdessemed, and K. Ghedamsi, **"Sliding mode control of a dual-stator induction generator for wind energy conversion systems,"** *Int. J. Electr. Power Energy Syst.*, vol. 42, no. 1, pp. 60–70, Nov. 2012, doi: 10.1016/j.ijepes.2012.03.024.

[32] H.-R. Jo, Y.-J. Kim, and K.-B. Lee, **"LCL-Filter Design Based on Modulation Index for Grid-Connected Three-Level Hybrid ANPC Inverters,"** *J. Electr. Eng. Technol.*, vol. 16, no. 3, pp. 1517–1525, May 2021, doi: 10.1007/s42835-021-00703-x.

[33] Y. Han *et al.*, **"Modeling and Stability Analysis of LCL-Type Grid-Connected Inverters: A Comprehensive Overview,"** *IEEE Access*, vol. 7, pp. 114975–115001, 2019, doi: 10.1109/ACCESS.2019.2935806.